Journal of Materials Chemistry C

Reactive Phosphine Combinatorial Co-Sputtering of Cation Disordered $ZnGeP_2$

Journal:	*Journal of Materials Chemistry C*
Manuscript ID	TC-ART-10-2021-004695.R1
Article Type:	Paper
Date Submitted by the Author:	22-Nov-2021
Complete List of Authors:	Schnepf, Rekha; Colorado School of Mines, Physics; National Renewable Energy Laboratory Crovetto, Andrea; Helmholtz-Zentrum Berlin fur Materialien und Energie GmbH, Department of Structure and Dynamics of Energy Materials; National Renewable Energy Laboratory Gorai, Prashun; Colorado School of Mines, Metallurgical and Materials Engineering; National Renewable Energy Laboratory, Park, Anna; National Renewable Energy Laboratory Holtz, Megan; Colorado School of Mines, Metallurgical and Materials Engineering Heinselman, Karen; National Renewable Energy Laboratory Bauers, Sage; National Renewable Energy Laboratory Tellekamp, Marshall; National Renewable Energy Laboratory Zakutayev, Andriy; National Renewable Energy Laboratory, Greenaway, Ann; National Renewable Energy Laboratory, Materials Chemistry Science & Technology Toberer, Eric; Colorado School of Mines; National Renewable Energy Laboratory Tamboli, Adele; National Renewable Energy Lab, ; Colorado School of Mines, Physics

SCHOLARONE™
Manuscripts

Journal Name

ARTICLE TYPE

Cite this: DOI: 00.0000/xxxxxxxxxx

Reactive Phosphine Combinatorial Co-Sputtering of Cation Disordered $ZnGeP_2$ Films†

Rekha R. Schnepf[a,b], Andrea Crovetto[b,c], Prashun Gorai[a,d], Anna Park[b], Megan Holtz[d], Karen N. Heinselman[b], Sage R. Bauers[b], M. Brooks Tellekamp[b], Andriy Zakutayev[a,d], Ann L. Greenaway[b], Eric S. Toberer[a,b] and Adele C. Tamboli*[a,b]

Received Date
Accepted Date

DOI: 00.0000/xxxxxxxxxx

The discovery of new materials by coupling high-throughput synthesis with computational screening is being increasingly adopted. However, thus far, phosphides have been largely overlooked for both computational screening and high-throughput synthesis. In this paper, we report on the use of a high-throughput synthesis technique, reactive combinatorial co-sputtering with PH_3, to deposit $ZnGeP_2$ thin films. We grew amorphous films over a wide range of compositions and found an upper limit in growth temperature determined by Zn and P volatility. We found that depositing in a Ge-limited regime could be utilized to slow the growth rate to compensate for the desorption of the Zn and P. Crystalline films were achieved by depositing films at higher temperatures in this Ge-limited regime with a reduced deposition rate. X-ray diffraction revealed that the films had crystallized in the zincblende, cation-disordered structure. The crystalline films exhibited optical absorption energy threshold values ranging from 0.8 to 1.3 eV. Increased Ge content was found in films that exhibited a decreased absorption onset energy. Native defect calculations were used to gain an understanding of the off-stoichiometry seen in these films. This work provides the first high-throughput investigation of $ZnGeP_2$, demonstrating the ability to grow amorphous and cation disordered $ZnGeP_2$ over a wide range of compositions with varying optical properties.

1 Introduction

There has been growing interest in discovering new ternary and multinary materials that will enable technological advances in optoelectronic devices through increased diversity in available chemistries and structures.[1–3] In order to focus materials discovery efforts on the most promising new materials, it is critical that there is close coordination between computational screening and materials synthesis.[4] For example, computational work on ternary nitrides has uncovered hundreds of new stable and metastable nitride materials providing experimentalists with guidance on new compounds to synthesize.[2] There has been much less exploration done in the phosphide space, with far fewer predicted phosphide compounds compared to nitrides, sulfides, and oxides.[3] Yet, in a study done to assess the properties of 171 existing phosphides in the Inorganic Crystal Structure Database (ICSD), the phosphide materials were predicted to have low effective masses and band gap energies in the ideal range for tandem photovoltaics (PV).[5] The very successful III-P alloys have been included in highly-efficient multijunction solar cells for several decades,[6] with efficiencies as high as 47%.[7] Studies on the less-explored ternary II-IV-V_2 phosphide materials, such as $ZnSiP_2$[8] and $ZnSnP_2$,[9] have also revealed their strong potential for solar cell device applications. Additionally there has been expanding work on cobalt phosphide[10] and other metal phosphide materials[11] for energy-related applications such as water splitting, fuel cells, batteries, and supercapacitors. The promising properties of existing phosphides suggest that unexplored phosphide materials could provide fertile ground for more extensive computational screening and synthetic experimentation. However, challenges related to the synthesis of phosphide thin films, such as the use of the hazardous PH_3 gas, have stunted high-throughput experimentation of phosphides.

High-throughput experimental techniques are a key component to the materials discovery process by enabling the generation of large amounts of experimental data using combinatorial material synthesis and rapid characterization techniques.[4,12] Combinatorial synthesis methods generate a large number of samples in a single deposition allowing for the fast and low-cost exploration of

[a] National Renewable Energy Laboratory, Golden, CO 80401, USA.
[b] Department of Physics, Colorado School of Mines, Golden, CO 80401, USA.
[c] Department of Structure and Dynamics of Energy Materials, Helmholtz-Zentrum Berlin für Materialien und Energie GmbH, Berlin, Germany
[d] Department of Metallurgical and Materials Engineering, Colorado School of Mines, Golden, CO 80401, USA.
* E-mail: adele.tamboli@nrel.gov; Fax: +1-303-384-7600; Tel: +1-303-384-7223.
† Electronic Supplementary Information (ESI) available

a material's phase space.[13] Combinatorial co-sputtering, in particular, is an already proven method to synthesize new II-IV-N_2 materials similar to $ZnGeP_2$. It has been used to explore the effects of off-stoichiometry on structure and optoelectronic properties in $ZnSnN_2$,[14] $ZnGeN_2$,[15] and $MgSnN_2$.[16] However, sputtering is a largely under-utilized synthesis technique for phosphides. There have been a few reports of sputtering from phosphide targets to achieve GaP[17–19] and Cu_3P films.[9] Reactive sputtering with PH_3 gas has been even less explored with only two studies on sputtered Zn_3P_2[20,21] and one on BP.[22] The development of a reactive combinatorial sputtering technique for phosphides could enable the rapid investigation of new phosphide materials, such as $ZnGeP_2$.

For this study, we have chosen to explore the viability of combinatorial phosphide synthesis using $ZnGeP_2$ due to its strong potential for optoelectronic devices. As a II-IV-P_2 material, $ZnGeP_2$ has the potential to exist in either a zinc-blende cation-disordered or a chalcopyrite cation-ordered structure. The cation-ordered structure is predicted to have a band gap of 2.2 eV.[23] However, previous experimental work indicates that cation site disorder can be used to lower its band gap to 1.7 eV,[24] the ideal band gap for a top cell absorber in a Si-based tandem solar cell.[25] In addition to having a tunable band gap, $ZnGeP_2$ is also lattice matched to Si, with a less than 1% lattice mismatch, making it a very promising material for integration in Si-based devices.[26] Despite promising initial reports on $ZnGeP_2$, the research on thin film synthesis of $ZnGeP_2$ remains sparse, with only a few reports of organometallic chemical vapor deposition[27,28] and low-pressure chemical vapor deposition with a combination of hydride and elemental precursors.[24,29] Employing a high-throughput growth method, such as combinatorial co-sputtering, could allow for expedited phase space exploration of $ZnGeP_2$.

In this study, we have achieved high-throughput phosphide thin film synthesis by depositing combinatorial $ZnGeP_2$ thin films via reactive RF co-sputtering in PH_3 gas. Amorphous films were produced over a range of compositions by utilizing lower deposition temperatures and higher deposition rates. Crystalline, cation-disordered $ZnGeP_2$ films were achieved by depositing films at higher temperatures with lower growth rates. Transmission electron microscopy (TEM) was utilized to investigate the microstructure of the films, revealing changes in crystallinity and composition depending on the growth conditions. Absorption coefficients were determined by modelling spectroscopic ellipsometry data, where a trend of decreased absorption onset with increased Ge content was discovered. Finally, native defect calculations shed light on the off-stoichiometric compositions of the experimental films.

2 Methods

2.1 Growth Methods

Eight thin film sample libraries were deposited using a PVD Products sputter deposition system, as shown in Fig. 1. This chamber utilizes radio frequency co-sputtering of metallic targets, Zn and Ge, while flowing dilute PH_3 gas (5% PH_3 in Ar) to deliver P to the chamber. The substrate heater and plasma formed during the sputter process are used to crack the PH_3 gas. For this study, the Zn and Ge sources were 2" metallic targets purchased from Kurt J. Lesker Company with 99.99% and 99.999% purity, respectively. The Zn and Ge sputter guns were angled at 22°to the substrate normal. The substrate was not rotated during the deposition to allow for a gradient in Zn and Ge fluxes, and thus composition, across the substrate. All of the films reported in this work were deposited at an operating pressure of 7 mTorr with 28 sccm of the 5% PH_3 in Ar gas mixture flowing into the chamber. Prior to these depositions the chamber base pressure ranged over $4-8\times10^{-7}$ Torr.

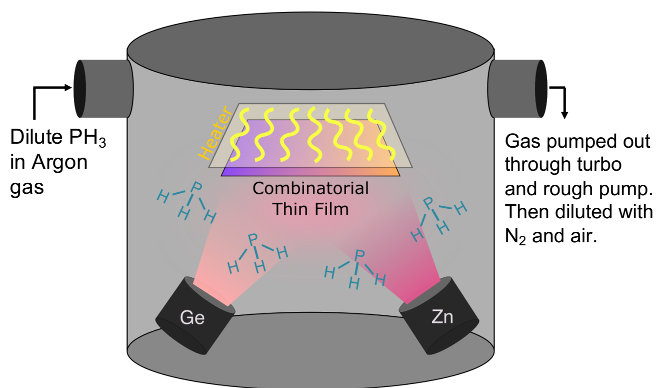

Fig. 1 A schematic of the vacuum chamber used to deposit the $ZnGeP_2$ films in this study. Metallic Zn and Ge targets were sputtered in a dilute PH_3 in Ar gas environment. The plasma formed during the sputter process was used to crack the PH_3 gas to provide reactive P. A lamp heater located above the substrate was used to control the substrate temperature during the deposition process.

Throughout this work, it was important to have safety protocols in place because PH_3 is both a toxic and pyrophoric gas. For these experiments, there were multiple points in the lab near the vacuum chamber and in the lab exhaust that were monitored for the presence of PH_3. If any PH_3 was detected, it would immediately trip an interlock for the growth system and shut off the flow of PH_3 to the growth chamber. During a deposition, unused PH_3 and Ar gas are safely removed from the chamber through a turbomolecular pump and then through a rough pump. Once through the rough pump, the exhaust is then diluted with nitrogen to less than 2% by volume. The diluted gases are then sent to a Pure Air Systems abatement system where they are mixed with room air in a controlled environment and then exhausted into the primary lab exhaust duct. When removing a sample from the chamber, a local ventilation snorkel was placed over the load lock in case of any phosphorous reactions when the sample was exposed to air. Additionally, self contained breathing apparatuses were worn by users whenever the chamber was vented because of solid P deposits on the chamber walls that react to form PH_3 when exposed to air.

The combinatorial $ZnGeP_2$ thin films were deposited on 2" x 2" p-type Si substrates with native oxide purchased from University Wafers. The Si substrates were soaked in acetone, isopropanol, and deionized water for 2 minutes each prior to loading the substrates into the sputter chamber. Prior to depositing on the substrate, the Zn and Ge targets were pre-sputtered for 30 minutes

with their shutters closed to remove any reacted surface layers and ensure run-to-run consistency. . The sputter gun powers were adjusted to reach a variety of cation compositions for the depositions being included in this report. The Zn target power ranged from 30 to 110 W. The higher Zn target powers were used at higher temperatures to counter increased Zn-desorption at increased substrate temperatures. The Ge target power ranged from 7 to 10 W. Lower Ge target powers were used to reach a Ge-limited growth regime (Zn and P-rich conditions) at high deposition temperatures when Zn and P have high vapor pressures. Substrate temperatures ranged from 310 to 410°C; these temperatures were calibrated using a thermocouple on a Si substrate. The deposition time varied from 2 to 5 hours, with the longer growth times used for depositions at lower growth rates achieved with the lowest Ge power used. Film thickness in the five amorphous films varied from 100 to 250 nm. In the crystalline films, the film thickness was maintained between 60 to 70 nm for all three samples reported here.

2.2 Characterization Methods

Each film was characterized as a sample library, containing a grid of 4x11 sample points, using a suite of spatially resolved characterization tools with mapping capability. These tools collect measurements at the same standardized positions for the 4x11 grid. The mapping data were then processed and analyzed in Igor Pro using the COMBIgor data analysis package.[30] X-ray diffraction (XRD) mapping was performed using a Bruker D8 Discover equipped with an area detector, using $\theta - 2\theta$ geometry and Cu Kα radiation, and General Area Detector Diffraction System software. Pawley refinements were performed on the XRD data using the TOPAS 6 Academic software package. The zincblende structure, F$\bar{4}$3m, was used as the base structure for the refinement. The data was fit with Gaussian and Lorentzian functions to account for peak broadening. Error bars for the lattice parameters were generated from TOPAS based on how well the refinement fit.

Film composition maps were collected using a Bruker M4 Tornado Micro-XRF spectrometer, using a Rh excitation beam and two detectors. The XRF spectra was then modeled to extract the film composition using the XMethods software package. Rutherford backscattering (RBS) measurements were conducted on three sample points and included in the XRF modeling in order to calibrate the XRF composition fitting. The RBS measurements were also used to verify that negligible amounts of oxygen were being incorporated in the films.

TEM was conducted on two of the crystalline samples to obtain information on film morphology, amorphous phase content, and film composition as a function of film depth. Bright field TEM images, High-angle annular dark-field scanning transmission electron microscopy (HAADF STEM) images, and energy dispersive spectroscopy (EDS) mapping were acquired on a ThermoFisher FEI Talos F200X equipped with a Super-X EDS system consisting of four silicon drift detectors. Cross-sectional specimens for TEM analysis were prepared using focused ion beam liftout, on a ThermoFisher FEI Helios NanoLab 600i, with a final ion-beam cleaning at 2kV to minimize surface amorphization.

Spectroscopic ellipsometry was performed to determine the absorption coefficient of the samples. The measurements were conducted on the first row of each sample library (11 points) using a J.A. Woollam Co. M-2000 variable angle ellipsometer at three angles: 65°, 70°, and 75°. These angles were chosen as they are close to the Brewster angle of Si, which is near 75°, in the wavelength range of the measurement. The CompleteEASE software (version 6.56) was used to create and fit optical models. The samples were modeled by fitting the imaginary part of the dielectric function with Cody-Lorentz, Lorentz, and PSemi-M0 oscillators.

2.3 Defect Calculations

We calculated the formation energy of native defects in $ZnGeP_2$ with the goal of understanding the site disorder, the propensity for off-stoichiometry in experimental films, and the presence of deep defects. We employed the standard supercell approach[31] to calculate the defect formation energy ($\Delta E_{D,q}$) given by,

$$\Delta E_{D,q} = E_{D,q} - E_{\text{host}} + \sum_i n_i \mu_i + qE_{\text{F}} + E_{\text{corr}} \quad (1)$$

where $\Delta E_{D,q}$ is the formation energy of a specific defect D in charge state q, $E_{D,q}$ and E_{host} are the total energy of the supercell with and without the defects, respectively. E_{F} is the Fermi energy, which varies between the valence band maximum (VBM) and the conduction band minimum (CBM), and E_{corr} is the term that accounts for the finite-size corrections due to the use of periodic supercells. The chemical potential of elemental species i is μ_i and n_i is the number of atoms of species i added ($n_i < 0$) or removed ($n_i > 0$) from the host supercell to form the defects. μ_i is expressed as $\mu_i = \mu_i^0 + \Delta\mu_i$, where μ_i^0 is the reference chemical potential and $\Delta\mu_i$ the deviation from the reference value. The bounds on $\Delta\mu_i$ are set by thermodynamic phase stability, with $\Delta\mu_i$ = 0 corresponding to i-rich conditions and a large negative value of μ_i representing i-poor growth conditions.

For the defect calculations, we built 216-atom supercells and calculated their total energy by fully relaxing the atomic positions (keeping the volume and cell shape fixed) with density functional theory (DFT). A plane-wave energy cutoff of 340 eV and Brillouin zone sampling using a Γ-centered $2 \times 2 \times 2$ $\vec{k}$ point grid was used to relax the supercells. DFT calculations were performed with the Vienna Ab Initio Simulation Package (VASP) software package.[32] The generalized gradient approximation (GGA) of Perdew-Burke-Ernzerhof (PBE) was used as the exchange correlation functional.[33] The core and valence electrons were treated with the projector-augmented wave (PAW) method.[34]

The native point defects considered include vacancies (V_{Zn}, V_{Ge}, V_P) and anti-site defects (Ge_{Zn}, Zn_{Ge}, Zn_P, P_{Zn}, Ge_P, P_{Ge}). We found in our previous work on $ZnSiP_2$ that interstitials are not low-energy defects.[8] The formation energy of these native point defects were calculated in charge states ranging from -3 to +3, with additional charge states considered where necessary. The reference chemical potentials (μ_i^0) were obtained by fitting to a set of experimentally measured formation enthalpies, similar to the procedure described in Ref. 35, which has been shown

to provide more accurate predictions of formation enthalpy and therefore, phase stability.

We computed the finite-size corrections with the Lany and Zunger[31] scheme, which includes the following corrections to $\Delta E_{D,q}$:(1) image charge correction for charged defects, (2) potential alignment correction for charged defects, and (3) band-filling corrections for shallow defects. Electronic structures calculated with GGA-PBE functional tends to severely underestimate the band gap of semiconductors. To rectify this issue, we also applied a band gap correction (through individual band edge shifts) based on GW quasi-particle energy calculations.[36] A computational framework for automating point defect calculations, pylada-defects[37], was used in this work for creating the defect supercells and analyses of the results, including calculation of the finite-size corrections.

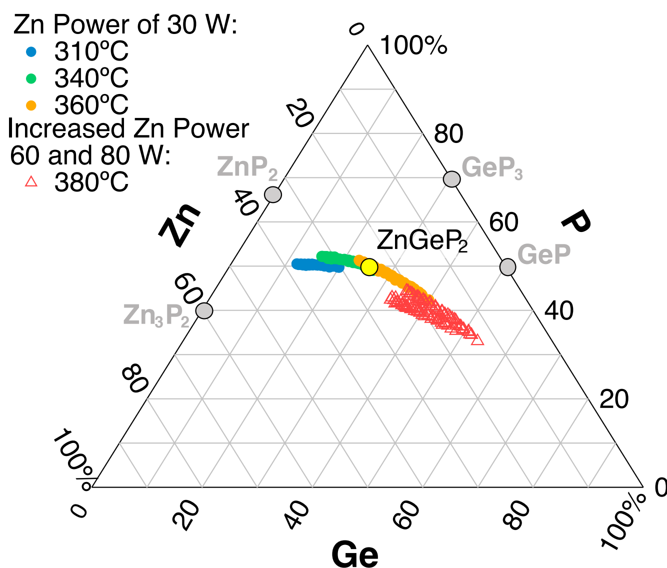

Fig. 2 Experimental ternary diagram for the amorphous films grown in this study. All 44 points of the sample libraries deposited at different temperatures are shown in different colors. The triangle marker is representative of samples grown with higher Zn powers. This figure highlights the wide range of compositions that were reached in these films, while also showing the propensity to lose Zn and P at higher temperatures.

3 Results

3.1 Amorphous Films

The reactive sputter deposition process, illustrated in Fig.1, yielded amorphous or crystalline thin films depending on the growth temperature and deposition rate. The amorphous films were deposited at growth temperatures ranging from 310°C to 380°C, with the Ge power held constant at 10 W. XRD data for these films, exhibiting the amorphous character and lack of peaks, can be found in Fig. S1 in the supplemental information. The amorphous films spanned a wide range of compositions, as shown in the ternary phase diagram in Fig. 2. From RBS, it was found that there was only 2 at.% of oxygen present on the Zn-rich side of the films and, on the Ge-rich side, the oxygen content was below the noise level. A decrease in Zn incorporation with increased temperature was found across all of the films, as shown in Fig. 2. The high vapor pressure of Zn at increased temperatures is the likely cause of this difficulty in maintaining a stoichiometric amount of Zn in the films grown at elevated temperatures. At high enough temperatures, such as 380°C, increasing the Zn power results in only negligible changes to the Zn content in the film due to the high rate of Zn desorption from the hot substrate.

As P is also a volatile element, a similar trend of increased substrate temperature and decreased P incorporation was discovered. At temperatures of 360°C and above, there is a decrease in P content in the films with increased growth temperature. However, unlike the Zn behavior, when increasing the temperature from 310°C to 340°C, there was a slight increase in P incorporation in the film. This increase in P incorporation is likely due to improved efficiency in cracking of the PH_3 gas at the substrate surface with the increased substrate temperature. However, when the substrate temperatures are above 360°C, the improved cracking efficiency is not enough to compensate for the desorption of P from the substrate surface. This decrease in both Zn and P content in the films grown at 360°C and above can be seen as a tilt in the data represented by the orange circles and red triangles towards the pure Ge endpoint in the ternary phase diagram in Fig. 2. A similar coupling of Zn and P content was found in amorphous $ZnSiP_2$-Si alloy thin films.[38] These films spanned a range of compositions but largely followed the $ZnSiP_2$-Si line on the ternary phase diagram. This behavior in the amorphous $ZnSiP_2$-Si films was attributed to the surface chemistry during growth driving towards a charge balanced (2P:Zn) composition, which could also be a factor contributing to the coupled nature of the Zn and P loss in the $ZnGeP_2$ films in this work.

3.2 Crystalline Films

Crystalline, cation disordered $ZnGeP_2$ samples were achieved by depositing in a Ge-limited regime with slower growth rates and at higher temperatures. Substrate temperatures of 380°C and above were used for these films. A Ge-limited regime and slower growth rates were achieved by lowering the Ge power from 10 W to 8 W, which resulted in a decrease in the deposition rate from 1.7 nm/min to 0.3 nm/min. These samples had oxygen levels that were below the RBS noise level. The XRF composition data for the first row of each crystalline library is shown in Fig.3. While the decreased growth rate compensated somewhat for the Zn and P desorption at the substrate surface, all of these films are still P poor with only marginal improvements in P content by further lowering the Ge power to 7 W. The samples deposited at the higher temperature of 400°C are Zn poor across all points on the sample library. The ability for II-IV-V_2 materials to crystallize into the cation disordered structures at off-stoichiometric cation compositions has already been experimentally realized in several II-IV-N_2 materials, such as $ZnSnN_2$,[14] $ZnGeN_2$,[15] and $MgSnN_2$.[16] The tendency for II-IV-V_2 materials to withstand variations in cation compositions is possibly due to the energetic favorability of antisite defects in these materials.[1]

In addition to off-stoichiometric cation compositions, we again see the simultaneous loss of Zn and P occurring in these films,

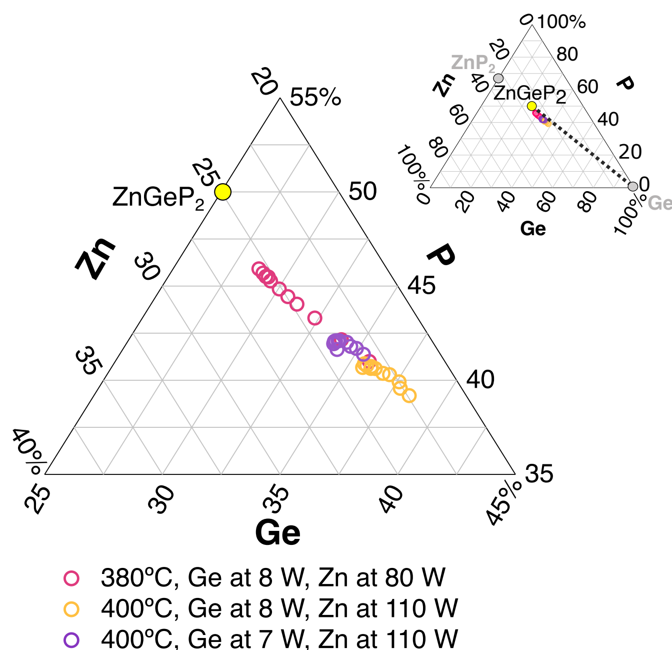

Fig. 3 Experimental ternary diagram for the crystalline samples. The smaller diagram on the top right shows the full axis ranges from 0 to 100%. A line is included in this plot to show that the composition spread follows the $ZnGeP_2$-Ge alloy line. The larger diagram shows the data with a narrower range on the axis to more clearly visualize the data points. Different sample libraries are shown in different colors.

with the composition data closely tracking the $ZnGeP_2$-Ge alloy line. This behavior is highlighted in the inset in Fig.3, where the data points are located near the line connecting $ZnGeP_2$ to the Ge endpoint in the phase diagram. Alloy-like behavior has also been revealed in the related nitride compound, cation disordered $ZnGeN_2$, where shifts in cell volume and absorption edge energy that are consistent with an alloy-like model for these parameters have been reported.[15] However, for the $ZnGeP_2$ films in this work, while the composition data is suggestive of a $ZnGeP_2$-Ge alloy forming, the TEM and XRD results indicate that this cannot be the sole explanation.

TEM microscopy revealed changes in the amorphous phase content and non-uniformity of the composition profiles with changes in the growth conditions. The TEM microscopy was conducted on two sample points, one point on the Zn-rich side of the sample deposited at 380°C (closest to stoichiometric) and the other point on the Ge-rich side of the sample deposited at 400°C with a Ge power of 8 W (XRF Ge content of 40 at%). The TEM cross sectional images and EDS depth profiles are displayed in Fig.4. In both films, there is an amorphous region near the Si substrate that is more Ge-rich than the rest of the film. This is consistent with the volatile elements, Zn and P, diffusing towards the film surface at the higher growth temperatures, resulting in a Ge-rich region at the substrate interface.[39] However, in the sample deposited at 400°C the amorphous region is significantly more Ge-rich than in the film deposited at 380°C. In the sample deposited at 380°C, there is an additional amorphous region near the top of the film. Contrary to the amorphous region near the Si substrate, the amorphous region at the top of the film is the same composition as the rest of the film. In both films, the crystalline regions have very consistent composition throughout that region. It should be noted that the atomic percents of Zn, Ge, and P determined from the EDS line scan for these points differ from the XRF values shown in Fig. 3. This difference is likely due to the larger sampling area in the XRF compared to the TEM EDS and the varied composition throughout the cross-section of the samples. Overall, the data from the TEM images and EDS analysis show that off-stoichiometry, in the form of excess Ge in the Ge-rich samples, exists in both the crystalline portion of the film and in the amorphous layers.

X-ray diffraction (XRD) data for these films support the conclusion that the disordered zinc-blende structure was formed during the deposition. Representative XRD patterns are shown in Fig.5 (a), with the color of the data traces representing the Ge content in the films. The reference patterns for the ordered and disordered structures are also plotted in Fig.5 (a). It can be seen that the XRD pattern for the ordered structure contains peak splitting in all of the peaks after 30°, while the disordered structure does not. The XRD patterns for the $ZnGeP_2$ samples lack the characteristic peak splitting of the ordered structure, instead matching the disordered XRD pattern. Pawley refinements were performed to extract the cubic zinc-blende lattice parameter, which is plotted in Fig.5 (b) as a function of Ge content. The lattice parameter results show that there is not a clear linear trend with Ge percent, as would be expected if there was a $ZnGeP_2$-Ge alloy forming. It is possible that there are slight tetragonal distortions in the crystal structure that aren't captured by fitting the data to the zincblende structure. However, fitting the XRD data with the tetragonal structure did not improve the goodness of fit for the model. From the TEM data, we have seen that there is varied composition throughout the films and excess Ge incorporating in both crystalline and amorphous regions. The information from both the TEM and Pawley refinements suggest that Ge is alloying with $ZnGeP_2$ in the crystalline regions of the film resulting in a larger lattice parameter. However, the non-uniformity of the microsctructure in each samples makes it difficult to establish a trend across all of the samples. Further optimization in synthesis will be needed to develop uniformly crystalline and stoichiometric films.

The absorption coefficient data supports the conclusion that the films are disordered and that varying Ge content can be used to tune the absorption onset energy. The absorption coefficient data is shown in Fig.6(a) with the color of the data trace indicating the Ge content in the films. The absorption onset energy across all of the samples is much lower, 1.3 to 0.8 eV, than what would be expected for fully ordered $ZnGeP_2$, 2.2 eV. This result is consistent with the previous work demonstrating a decrease in absorption onset energy with increased disorder in $ZnGeP_2$ thin films.[24] The absorption coefficient data for a previously published film with a long range order parameter, s, of 0.51(1)[24] is included in the plot in Fig. 6 (a) to highlight that the films in this work have even lower absorption onset energies. This result indicates that these films would likely have lower long-range order parameters corresponding to more disordered cation-site occupancies on av-

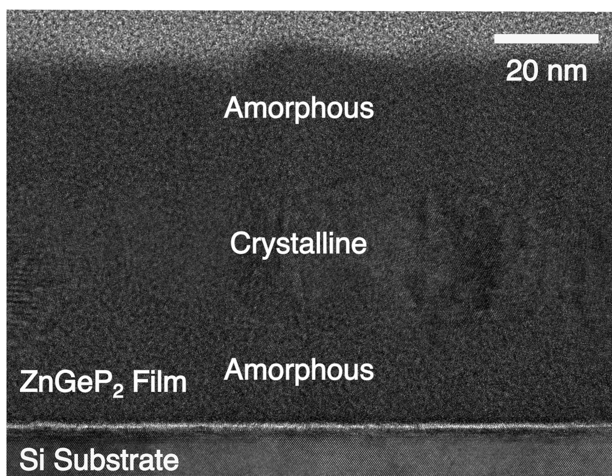

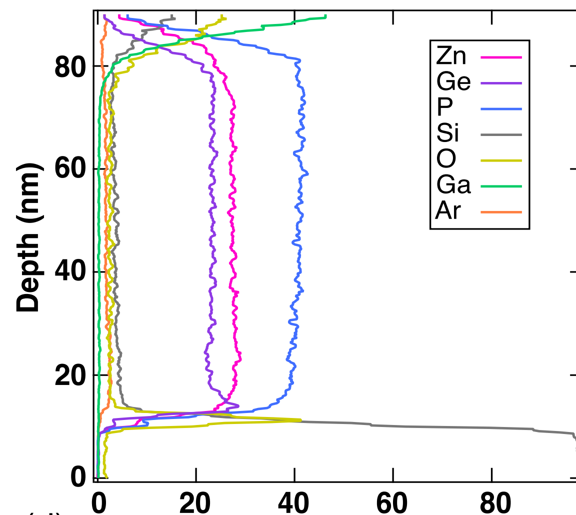

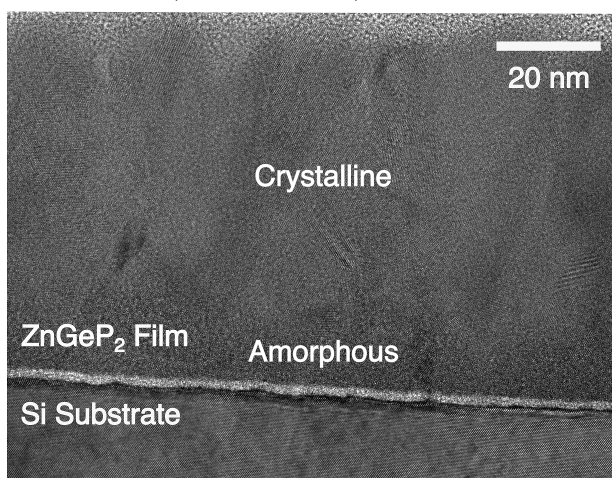

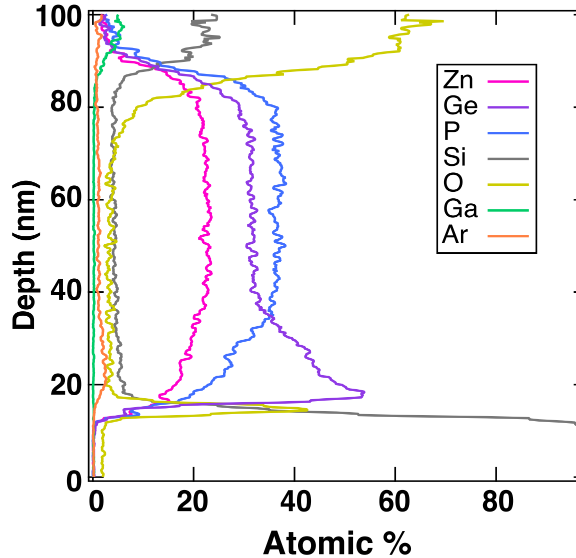

Fig. 4 (a) TEM cross-sectional image and (b) EDS line scan for the film deposited at 380°. (c) TEM cross-sectional image and (d) EDS line scan for the film deposited at 400°C.

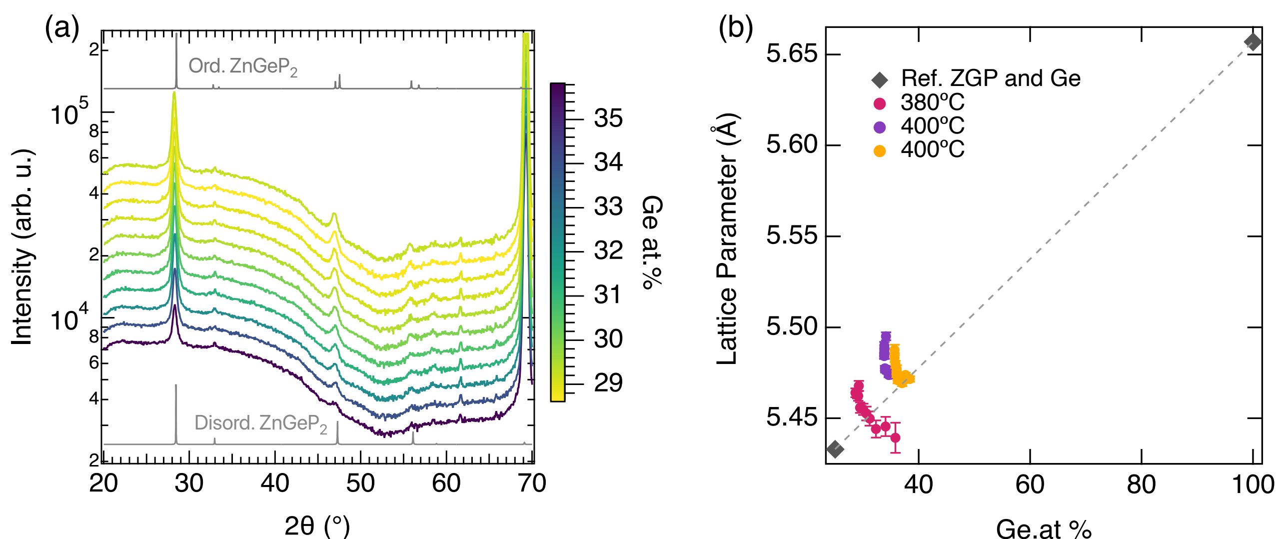

Fig. 5 (a) Representative XRD data for the crystalline $ZnGeP_2$ samples included in the work. The XRD data is plotted on a log scale. Reference ordered and disordered XRD patterns are included. Due to the lack of peak splitting in the experimental data, it is concluded that the disordered structure was formed. (b) Pawley refinements results showing the lattice parameter as a function of Ge content in the films. The reference lattice parameters for disordered $ZnGeP_2$ [40] and Ge [41] are included in the plot at the relevant Ge atomic percent.

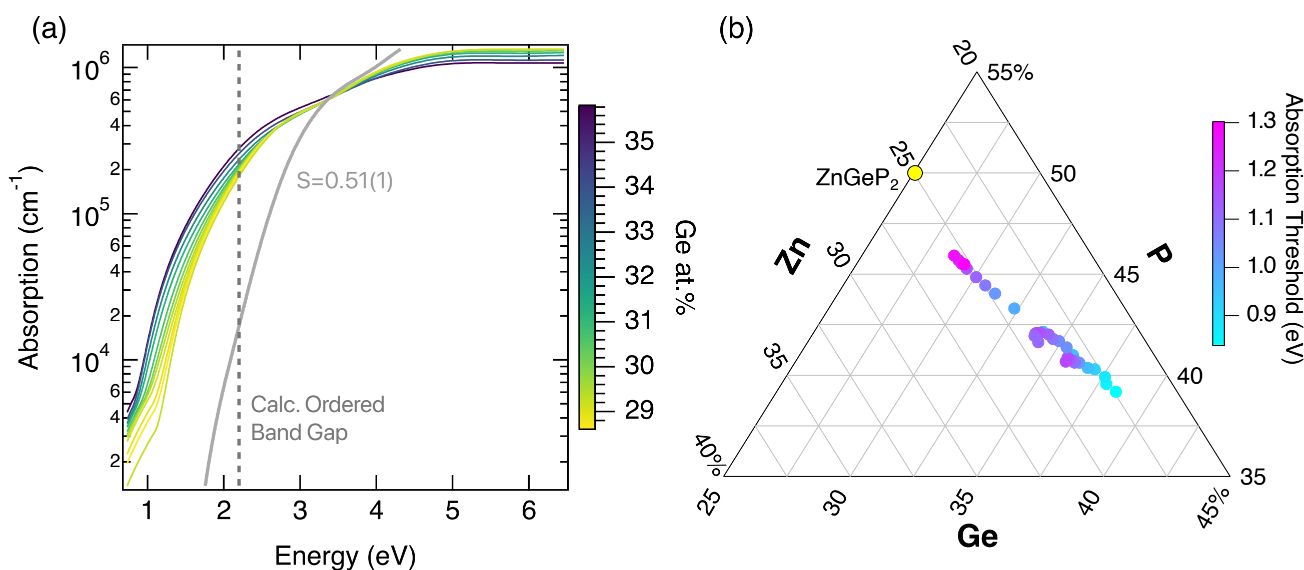

Fig. 6 (a) Representative experimental absorption coefficient data for the films included in this work. A trend in decreased absorption onset data with increased Ge content can be seen in the data. The calculated band gap for ordered $ZnGeP_2$ and the absorption coefficient for $ZnGeP_2$ with a long range order parameter, (s), of 0.51(1) are also included.[24] The lower absorption onset energy for the films in this work support the conclusion that they have formed in the cation disordered structure. (b) Experimental ternary diagram for the crystalline samples with marker color indicating the absorption threshold energy. The absorption threshold energy is the energy at which the absorption coefficient reaches a value of 10^4. This diagram highlights the decrease in the decrease in absorption threshold with an increasingly Ge-rich composition.

erage. Additionally, there is also a trend in decreased absorption onset energy with increased Ge content, as illustrated by the color spectrum in Fig.6 (a). The band gap of crystalline Ge is known to be 0.66 eV, so this might explain the resulting decrease in absorption onset energy in Ge-rich films. This trend is even more clearly visualized in Fig. 6(b) where the absorption threshold energy, the energy at which the absorption coefficient reaches the 10^4 value, is plotted as the marker color on the ternary phase diagram. Fig. 6(b) highlights the decrease in absorption threshold energy, from 1.3 to 0.8 eV, as the films become more Ge rich and Zn and P deficient. These results suggest that in $ZnGeP_2$ there is the additional possibility to tune optical properties through off-stoichiometry and Ge content. However, it should be noted that the inclusion of an amorphous Ge-rich layer could also be contributing to this trend in absorption onset energy.

Electrical measurements were attempted on the crystalline $ZnGeP_2$ films, however the films were too resistive to obtain consistent data. These findings are consistent with previous experiments in the literature on bulk $ZnGeP_2$ samples, which found the material to have carrier concentrations ranging from 10^{10}-10^{17} cm^{-3}.[26,42] Further experimentation on how electrical properties might change with doping and cation ordering are needed to further shed light on the electrical properties of $ZnGeP_2$.

3.3 Points Defects and Disorder

In order to understand how native point defects might allow for $ZnGeP_2$ to exist at off-stochiometric compositions, theoretical calculations were performed to determine the formation energy of various native point defects. The ternary phase stability map of Zn-Ge-P phases in chemical potential space is shown in Fig.7(a). The $ZnGeP_2$ stability region is bounded by the binary compounds GeP, GeP_3, ZnP_2, and Zn_3P_2. To account for various experimental growth regimes, the formation energy of native defects were calculated at multiple corners of the $ZnGeP_2$ phase stability region, labelled 1 through 5 in Fig.7(a). The films in this study were all Ge-rich ($\Delta\mu_{\mathrm{Ge}} = 0$ eV) and P-poor, which corresponds to conditions near points 1 and 2. The defect diagrams for points 1 and 2 are shown in Fig.7(c) and 7(d) with the equilibrium Fermi energy labelled. The defect energetics at other corners of the phase stability region can be found in the supplemental information. The equilibrium Fermi energy was calculated for a temperature of 400°C to match the synthesis temperatures of the films in this study. From Fig.7(c) and 7(d) it can be seen that the equilibrium Fermi energy lies near the mid-gap, suggesting charge compensation. The free carrier concentration calculated at all five points ranged from 10^{11} to 10^{13}, which also supports the experimental finding that the samples are insulating.

To assess the prevalence of the more energetically favorable point defects in $ZnGeP_2$, Fig.7(b) illustrates the concentration of four different point defects at each of the corner points from the chemical potential space map. The defect concentrations shown in Fig.7(b) were calculated at a temperature of 673K to match the synthesis temperature of 400°C. However, due to the non-equilibrium and energetic nature of sputtering the effective temperature associated with the growth process is likely much higher than 400°C.[43] As a result, the exact numbers plotted in Fig.7(b) are an underestimate of the defect concentrations in these films. However, the trends shown in Fig.7(b) remain the same at increased temperatures and a plot of the defect concentrations at an effective temperature of 1000K can be found in Fig. S4 in the supplemental information. In Fig.7(b), it can be seen that at points 1 and 2, Ge on Zn antisite (Ge_{Zn}) and Ge on P antisite (Ge_P) are the two most favorable defects and they are present at significantly higher concentrations than Zn on Ge (Zn_{Ge}) or P on Ge (P_{Ge}) anti-sites. The favorability of Ge antisite defects on both the cation and anion sites provides another possible mechanism for the ability to form $ZnGeP_2$ at the Ge-rich compositions shown in this paper. With this knowledge from the point defect calculations, it is likely that excess Ge, in the $ZnGeP_2$ samples reported here, is incorporating in Ge-rich amorphous regions and as a Ge-$ZnGeP_2$ alloy aided by the favorability of the Ge antisite defects.

Additionally, as shown in Fig.7(c) and (d), Ge_P and Ge_{Zn} antisites are deep defects. Deep defect levels arising from acceptor Ge_P antisites are present around 1 eV above the valence band edge and multiple defect levels for donor Ge_{Zn} antisite around 0.6-0.8 eV below the conduction band edge. The presence of a transition level around 1 eV above the valence band maximum seems to be consistent with the absorption onset observed in our samples (Fig. 6). Our calculated defect energetics qualitatively agree with previously published studies,[44–46] which also find the presence of high concentrations of Ge_P and Ge_{Zn} antisite defects with deep levels. The quantitative differences in the defect concentrations is attributed to the the differences in the DFT functionals used and more importantly, the thermodynamic phase stability. Unlike Ref. 44, we find that GeP and GeP_3 are stable phases i.e., they lie on the convex hull, which is due to the use of fitted elemental phase reference energies (see Methods Section) that is known to provide better estimates of formation enthalpy.[35]

Deep defects are undesired in photovoltaic absorbers because they act as centers for non-radiative carrier recombination.[47,48] Fig.7(b) also provides information on which growth regimes would result in lower concentrations of the deep antisite defects. For example, at points 3, 4, and 5, which correspond to more Ge-poor conditions, the concentration of Ge antisite defects is decreased by two orders of magnitude. However, further work on the experimental synthesis of $ZnGeP_2$ is needed to access the Zn and P-rich growth regimes.

4 Conclusions

In this work, we have demonstrated the growth of combinatorial amorphous and cation-disordered crystalline $ZnGeP_2$ thin films using reactive sputtering with PH_3 gas. Amorphous films were grown over a wide range of compositions showing the potential to grow compositionally tunable phosphides with this growth method. An upper limit in the substrate temperature was determined by the volatility of Zn and P. However, we found that operating in a Ge-limited regime by lowering the Ge power could be utilized to slow down the growth rate and compensate for the desorption of the Zn and P. Ge-rich crystalline films were achieved by depositing the films at higher temperatures in this Ge-limited

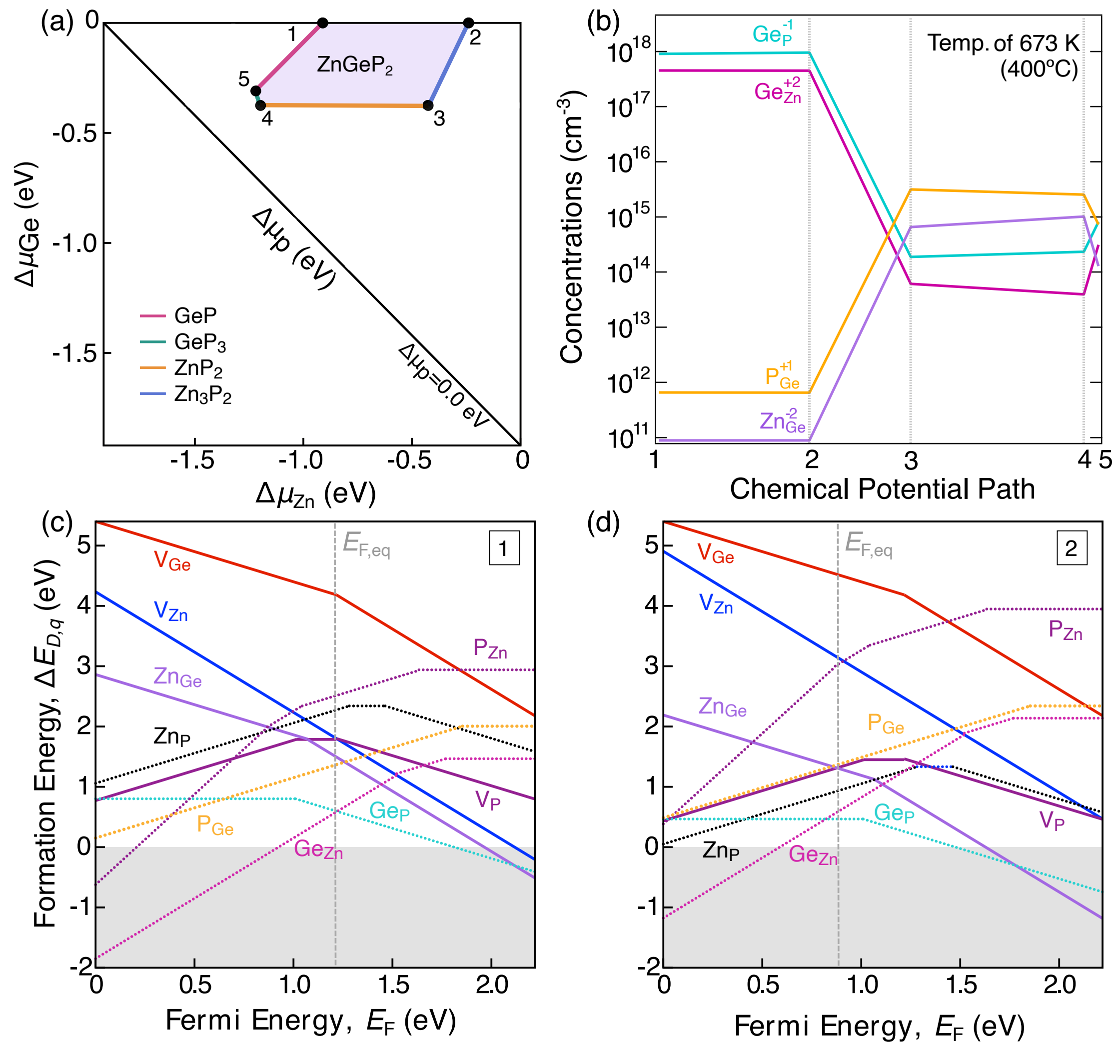

Fig. 7 (a) Chemical potential stability phase diagram for $ZnGeP_2$. (b) Defect diagram depicting the changes in concentration of various point defects along the five points in chemical potential space labelled in (a). The distances between the points on the x-axis are the Euclidean distances in the ternary chemical potential space defined by $\Delta\mu_{Zn}$, $\Delta\mu_{Ge}$, and $\Delta\mu_{P}$. (c)-(d) Defect formation energy plots corresponding to points 1 and 2 shown in (a), which are in a Ge-rich environment. The Fermi energy is referenced to the valence band maximum and the equilibrium Fermi energy, calculated at 400°C, is shown with the gray dashed line.

regime. Point defect calculations found Ge on the Zn site and Ge on the P site to be favorable defects, providing a possible explanation for the excess Ge in crystalline films. The crystalline $ZnGeP_2$ films exhibited absorption energy threshold values ranging from 1.3 to 0.8 eV. A decreased absorption threshold energy was found to trend with increased Ge content in the films. While there is significant work remaining to optimize synthesis conditions, these results highlight the strong potential for exploring phosphide materials using a combinatorial approach.

Author contributions

R.R.S. carried out the synthesis of the $ZnGeP_2$ films and primary characterization. A.C. aided in synthesis, maintaining the deposition chamber, and performed XRF analysis. P.G. completed the defect calculations and aided in the writing of the defect calculation sections of the manuscript. A.P. conducted the Pawley refinements. M.H. conducted the TEM characterization of the films. K.N.H. carried out the RBS measurements and analysis. S.R.B. performed electronic characterization of the films. A.C.T. and A.Z. contributed to the initial development and installation of the phosphide deposition chamber. R.R.S., A.C., S.R.B., M.B.T., A.Z., A.L.G, E.S.T, and A.C.T all contributed to developing and optimizing growth conditions. A.C.T was responsible for funding acquisition and is the project PI at NREL. A.C.T., E.S.T., A.L.G., and R.R.S were all involved in the project administration. R.R.S. wrote the majority of the manuscript, and all other authors provided feedback.

Conflicts of interest

There are no conflicts to declare.

Acknowledgements

Primary funding was provided by the U.S. Department of Energy, Office of Science, Basic Energy Sciences, Materials Sciences and Engineering Division. This work was authored in part by the National Renewable Energy Laboratory, operated by Alliance for Sustainable Energy, LLC, for the U.S. Department of Energy (DOE) under Contract No. DE-AC36-08GO28308. R. R. S. acknowledges support from the National Science Foundation Graduate Research Fellowship under Grant No. 1646713. EST acknowleges support from NSF DMR 1555340. The research was performed using computational resources sponsored by the Department of Energy's Office of Energy Efficiency and Renewable Energy and located at the NREL. The views expressed in the article do not necessarily represent the views of the DOE or the U.S. Government.

Notes and references

1 R. R. Schnepf, J. J. Cordell, M. B. Tellekamp, C. L. Melamed, A. L. Greenaway, A. Mis, G. L. Brennecka, S. Christensen, G. J. Tucker, E. S. Toberer, S. Lany and A. C. Tamboli, *ACS Energy Letters*, 2020, **5**, 2027–2041.

2 W. Sun, C. J. Bartel, E. Arca, S. R. Bauers, B. Matthews, B. Orvañanos, B.-R. Chen, M. F. Toney, L. T. Schelhas, W. Tumas, J. Tate, A. Zakutayev, S. Lany, A. M. Holder and G. Ceder, *Nature Materials*, 2019, **18**, 732–739.

3 A. L. Greenaway, C. L. Melamed, M. B. Tellekamp, R. Woods-Robinson, E. S. Toberer, J. R. Neilson and A. C. Tamboli, *Annual Review of Materials Research*, 2021, **51**, 591–618.

4 M. L. Green, C. L. Choi, J. R. Hattrick-Simpers, A. M. Joshi, I. Takeuchi, S. C. Barron, E. Campo, T. Chiang, S. Empedocles, J. M. Gregoire, A. G. Kusne, J. Martin, A. Mehta, K. Persson, Z. Trautt, J. Van Duren and A. Zakutayev, *Applied Physics Reviews*, 2017, **4**, 011105.

5 J. B. Varley, A. Miglio, V.-A. Ha, M. J. van Setten, G.-M. Rignanese and G. Hautier, *Chemistry of Materials*, 2017, **29**, 2568–2573.

6 M. Green, E. Dunlop, J. Hohl-Ebinger, M. Yoshita, N. Kopidakis and X. Hao, *Progress in Photovoltaics: Research and Applications*, 2021, **29**, 3–15.

7 J. F. Geisz, R. M. France, K. L. Schulte, M. A. Steiner, A. G. Norman, H. L. Guthrey, M. R. Young, T. Song and T. Moriarty, *Nature Energy*, 2020, **5**, 326–335.

8 A. D. Martinez, E. L. Warren, P. Gorai, K. A. Borup, D. Kuciauskas, P. C. Dippo, B. R. Ortiz, R. T. Macaluso, S. D. Nguyen, A. L. Greenaway, S. W. Boettcher, A. G. Norman, V. Stevanovic, E. S. Toberer and A. C. Tamboli, *Energy Environ. Sci.*, 2016, **9**, 1031–1041.

9 T. Kuwano, R. Katsube, K. Kazumi and Y. Nose, *Solar Energy Materials and Solar Cells*, 2021, **221**, 110891.

10 J. Wang, Z. Liu, Y. Zheng, L. Cui, W. Yang and J. Liu, *J. Mater. Chem. A*, 2017, **5**, 22913–22932.

11 X. Wang, H.-M. Kim, Y. Xiao and Y.-K. Sun, *J. Mater. Chem. A*, 2016, **4**, 14915–14931.

12 W. F. Maier, K. Stowe and S. Sieg, *Angewandte Chemie International Edition*, 2007, **46**, 6016–6067.

13 P. J. McGinn, *ACS Combinatorial Science*, 2019, **21**, 501–515.

14 A. N. Fioretti, A. Zakutayev, H. Moutinho, C. Melamed, J. D. Perkins, A. G. Norman, M. Al-Jassim, E. S. Toberer and A. C. Tamboli, *J. Mater. Chem. C*, 2015, **3**, 11017–11028.

15 C. L. Melamed, J. Pan, A. Mis, K. Heinselman, R. R. Schnepf, R. Woods-Robinson, J. J. Cordell, S. Lany, E. S. Toberer and A. C. Tamboli, *J. Mater. Chem. C*, 2020, **8**, 8736–8746.

16 A. L. Greenaway, A. Loutris, K. N. Heinselman, C. L. Melamed, R. R. Schnepf, M. B. Tellekamp, R. Woods-Robinson, R. Sherbondy, D. J. Bardgett, S. R. Bauers, A. Zakutayev, S. T. Christensen, S. Lany and A. Tamboli, *Journal of the American Chemical Society*, 2020, 8421–8430.

17 J. Sosniak, *Journal of Vacuum Science and Technology*, 1970, **7**, 110–114.

18 K. Starosta, J. Zelinka, D. BerkovÃi and J. Kohout, *Thin Solid Films*, 1979, **61**, 241–248.

19 Y. Li and Z. Liu, *Journal of Materials Science & Technology*, 2010, **26**, 93–96.

20 T. Suda, T. Miyakawa and S. Kurita, *Journal of Crystal Growth*, 1988, **86**, 423–429.

21 A. Weber, P. Sutter and H. von KÃ€nel, *Journal of Non-Crystalline Solids*, 1993, **164-166**, 79–82.

22 Z. Jia, J. Zhu, C. Jiang, W. Shen, J. Han and R. Chen, *Applied Surface Science*, 2011, **258**, 356–360.

23 *High Performance Computing Center Materials Database*, materials.nrel.gov.

24 R. R. Schnepf, B. L. Levy-Wendt, M. B. Tellekamp, B. R. Ortiz, C. L. Melamed, L. T. Schelhas, K. H. Stone, M. F. Toney, E. S. Toberer and A. C. Tamboli, *J. Mater. Chem. C*, 2020, **8**, 4350–4356.

25 T. J. Coutts, J. S. Ward, D. L. Young, K. A. Emery, T. A. Gessert and R. Noufi, *Progress in Photovoltaics: Research and Applications*, 2003, **11**, 359–375.

26 A. D. Martinez, A. N. Fioretti, E. S. Toberer and A. C. Tamboli, *J. Mater. Chem. A*, 2017, **5**, 11418–11435.

27 G. Xing, K. Bachmann, G. Solomon, J. Posthill and M. Timmons, *Journal of Crystal Growth*, 1989, **94**, 381 – 386.

28 G. C. Xing, K. J. Bachmann, J. B. Posthill and M. L. Timmons, *Journal of Applied Physics*, 1991, **69**, 4286–4291.

29 R. R. Schnepf, A. D. Martinez, J. S. Mangum, L. T. Schelhas, E. S. Toberer and A. C. Tamboli, 2019 IEEE 46th Photovoltaic Specialists Conference (PVSC), 2019, pp. 1052–1055.

30 K. R. Talley, S. R. Bauers, C. L. Melamed, M. C. Papac, K. N. Heinselman, I. Khan, D. M. Roberts, V. Jacobson, A. Mis, G. L. Brennecka, J. D. Perkins and A. Zakutayev, *ACS Combinatorial Science*, 2019, **21**, 537–547.

31 S. Lany and A. Zunger, *Phys. Rev. B*, 2008, **78**, 235104.

32 G. Kresse and J. Furthmüller, *Physical Review B*, 1996, **54**, 11169.

33 J. P. Perdew, K. Burke and M. Ernzerhof, *Physical Review Letter*, 1996, **77**, 3865.

34 P. E. Blöchl, *Physical Review B*, 1994, **50**, 17953.

35 V. Stevanović, S. Lany, X. Zhang and A. Zunger, *Phys. Rev. B*, 2012, **85**, 115104.

36 H. Peng, D. O. Scanlon, V. Stevanovic, J. Vidal, G. W. Watson and S. Lany, *Phys. Rev. B*, 2013, **88**, 115201.

37 A. Goyal, P. Gorai, H. Peng, S. Lany and V. Stevanovic, *Comp. Mater. Sci.*, 2017, **130**, 1.

38 A. D. Martinez, E. M. Miller, A. G. Norman, R. R. Schnepf, N. Leick, C. Perkins, P. Stradins, E. S. Toberer and A. C. Tamboli, *J. Mater. Chem. C*, 2018, **6**, 2696–2703.

39 M. Olgar, J. Klaer, R. Mainz, S. Levcenco, J. Just, E. Bacaksiz and T. Unold, *Thin Solid Films*, 2016, **615**, 402–408.

40 A. Vaipolin, E. Osmanov and V. Prochukhan, *Izvestiya Akademii Nauk SSSR,Neorganicheskie Materialy*, 1972, **8**, 947–949.

41 A. S. Cooper, *Acta Crystallographica*, 1962, **15**, 578–582.

42 H. M. Hobgood, T. Henningsen, R. N. Thomas, R. H. Hopkins, M. C. Ohmer, W. C. Mitchel, D. W. Fischer, S. M. Hegde and F. K. Hopkins, *Journal of Applied Physics*, 1993, **73**, 4030–4037.

43 P. F. Ndione, Y. Shi, V. Stevanovic, S. Lany, A. Zakutayev, P. A. Parilla, J. D. Perkins, J. J. Berry, D. S. Ginley and M. F. Toney, *Advanced Functional Materials*, 2014, **24**, 610–618.

44 M. Huang, S.-S. Wang, Y.-N. Wu and S. Chen, *Phys. Rev. Applied*, 2021, **15**, 024035.

45 X. Jiang, M. S. Miao and W. R. L. Lambrecht, *Phys. Rev. B*, 2005, **71**, 205212.

46 X. Jiang, M. S. Miao and W. R. L. Lambrecht, *Phys. Rev. B*, 2006, **73**, 193203.

47 W. Shockley and W. T. Read, *Phys. Rev.*, 1952, **87**, 835–842.

48 R. N. Hall, *Phys. Rev.*, 1952, **87**, 387–387.